



CdS-Cu_{1.81}S heteronanorods with continuous sublattice for photocatalytic hydrogen production

Sheng Liu^{a,d}, Xueyi Guo^{a,d,*}, Weijia Wang^{b,c,d,*}, Ying Yang^{a,d}, Congtan Zhu^{a,d},
Chongyao Li^{a,d}, Weihuang Lin^{a,d}, Qinghua Tian^{a,d}, Yong Liu^{c,d}

^a School of Metallurgy and Environment, Central South University, Changsha 410083, China

^b Institute of Clinical Medicine, the Second Affiliated Hospital of Hainan Medical University, Haikou 570311, China

^c State Key Laboratory for Powder Metallurgy, Powder Metallurgy Research Institute, Central South University, Changsha 410083, China

^d Research Institute of Resource Recycling, Central South University, Changsha 410083, China

ARTICLE INFO

Keywords:

CdS-Cu_{1.81}S heteronanorods (HNRS)
Cation exchange reaction
Continuous sublattice
Nanoheterostructures (NHs)
Photocatalytic hydrogen evolution reaction (HER)

ABSTRACT

Photocatalytic hydrogen (H₂) production is a cascade reaction that involves multiple limiting steps, such as light-harvesting, charge separation and transfer, redox reaction rate, and so on. Thus, there is a need to optimize each reaction node to promote the photocatalytic H₂ production efficiency for the commercial application of sustainable energy. Herein, we report integrally designed CdS-Cu_{1.81}S heteronanorods (HNRS) for photocatalytic H₂ production driven by near-infrared to ultraviolet irradiation. The intraparticle *p-n* junction and the well-constructed heterointerface result in highly efficient charge separation and transfer between the heterogeneous domains. Further adjusting the redox reaction sites on the surface of CdS-Cu_{1.81}S HNRS leads to a high photocatalytic H₂ production rate of 2.714 mmol·h⁻¹·g⁻¹, representing 150-fold and 108-fold improvements compared with pristine Cu_{1.81}S and CdS nanorods (NRs), respectively. Our work provides an alternative entry point for boosting the performance of noble-metal-free photocatalyst and highlights the importance of synergetic design.

1. Introduction

For the reason of the worsening environmental condition and global energy crisis, scientists are seeking sustainable and clean energy solutions [1–4]. Directly converting solar energy into chemical energy and storing it in the form of chemical bonds has aroused enormous attention [5–7]. Hydrogen (H₂), a versatile chemical mediator, not only can be used for electricity generation by combustion and hydrogen fuel cells but also can be used as a reducing agent for green pyrometallurgical production of metal raw materials [8,9]. Photocatalytic hydrogen evolution from water splitting thus becomes a promising approach among masses of sustainable energy solutions based on solar-to-chemical conversion [10,11].

An efficient photocatalytic hydrogen evolution reaction (HER) calls for clear-cut properties of photocatalysts [12,13]. An ideal photocatalyst should possess specific compositional and structural features, such as 1) broadband absorption for efficient light-harvesting, 2) neat interfaces and a high degree of crystallinity for effective charge transfer and low charge recombination, 3) a built-in electric field for effective

electron-hole separation, and 4) recycling considerations for a low material cost [14–17]. Hence, to extend the absorption spectra of the photocatalyst, materials with excellent ultraviolet-visible-near-IR (UV–vis–NIR) absorption features should be included [18,19]. To reduce interfacial lattice strain and/or defects, continuous sublattice should be constructed [20]. To enhance electron-hole separation, a *p-n* junction is needed [21,22]. To lower the cost, noble metal components (e.g. Au, Ag, and Pt) should be excluded, and the photocatalyst should be easy to fabricate and decompose [23,24].

So far, numerous creative strategies, such as interface and surface engineering, heterogenization, and the like, have been applied to modify the photocatalyst, expecting to maximize the efficiency of photon utilization [25–27]. Typically, single atomic or elemental state cocatalysts deposition on substrated catalysts introduces more reactive sites [28, 29]. Construction of heterostructures by epitaxial growth can facilitate spatial charge separation and adjust the band-edge potentials [30,31]. A noble-metal-free catalytic system contributes to the low cost of H₂ production [32,33]. Nevertheless, current modification tactics for photocatalysts have yet been sufficient to enhance H₂ production from the

* Corresponding authors at: Research Institute of Resource Recycling, Central South University, Changsha 410083, China.

E-mail addresses: xyguo@csu.edu.cn (X. Guo), wangweijia@csu.edu.cn (W. Wang).

<https://doi.org/10.1016/j.apcatb.2021.120909>

Received 14 August 2021; Received in revised form 13 October 2021; Accepted 5 November 2021

Available online 11 November 2021

0926-3373/© 2021 Elsevier B.V. All rights reserved.

challenge of giant electron-hole recombination loss which is resulted from lattice strain and defects at the heterointerface [31]. To address this issue, high-crystalline-quality photocatalysts with precisely constructed interfaces are required [34,35]. Moreover, how to integrate the features of an ideal photocatalyst into a simple catalytic system is still a challenge [36].

Herein, we report an active solar-light-driven catalyst based on single-particulate CdS-Cu_{1.81}S heteronanorods (HNRs) for H₂ production via water splitting. Cd²⁺ has been integrated into the sublattice of Cu_{1.81}S NRs by a stoichiometrically limited cation exchange reaction [37–39], obtaining CdS-Cu_{1.81}S HNRs with distinguishing domains of roxbyite Cu_{1.81}S and greenockite CdS, continuous anion skeleton, and engineered interfaces at atomic precision. This *in situ* integration of *n*-type CdS and *p*-type Cu_{1.81}S is expected not only to establish a built-in electric field for spatial charge separation but also to construct perfect interfaces for fast charge transfer as well as to enhance broadband absorption. Moreover, because of their simple structures, CdS-Cu_{1.81}S photocatalysts can be recycled easily through solvent extraction. By varying the Cu_{1.81}S/CdS content ratio and aspect ratio, the H₂ production efficiency of HNRs can be tuned accordingly. The optimal H₂ production efficiency of the CdS-Cu_{1.81}S HNRs is 2.714 mmol·h⁻¹·g⁻¹, representing 150-fold and 108-fold improvements compared with pristine Cu_{1.81}S and CdS NRs, respectively. Our work provides an alternative and promising approach for further improving the H₂ production efficiencies of semiconductor-semiconductor type photocatalysts via precisely constructing the heterointerfaces, as well as synergetically designing the shapes, sizes, and heterogeneous domain distributions of the nanocatalysts.

2. Experimental section

2.1. Chemicals and materials

Copper (II) nitrate trihydrate [Cu(NO₃)₂·3H₂O, 99%], cadmium chloride [CdCl₂, 99.99%, metal basis], anhydrous sodium sulfite [Na₂SO₃, ≥ 98%, ACS reagent grade], sodium sulfide nonahydrate [Na₂S·9H₂O, ≥ 98%, AR grade], *tert*-dodecanethiol [*t*-DDT, C₁₂H₂₆S, 98%, mixture of isomers], 1-octadecene [ODE, C₁₈H₃₆, > 90%, GC grade], formamide [FMM, CH₃NO, ≥ 99.5%, ACS reagent grade], and β-mercaptopropionic acid [MPA, C₃H₆O₂S, 98%] were purchased from Aladdin. Oleylamine [OLAM, C₁₈H₃₇N, ≥ 98% (primary amine)] was purchased from Sigma-Aldrich. Anhydrous sodium sulfate [Na₂SO₄, 99%, AR grade] and trioctylphosphine [TOP, C₂₄H₅₁P, 90%] were purchased from Macklin. Anhydrous ethanol [C₂H₆O, ≥ 99.5%, AR grade] and *n*-hexane [C₆H₁₄, > 99%, ACS reagent grade] were purchased from Sinopharm. Tri-*n*-octylphosphine oxide [TOPO, C₂₄H₅₁PO, 98%] was purchased from two different manufacturers (Aladdin and Macklin). TOPO-A and TOPO-M represent the products that were purchased from Aladdin and Macklin, respectively. Unless otherwise specified, all chemicals were used as received without further purification.

2.2. Synthesis of roxbyite Cu_{1.81}S NRs

The roxbyite Cu_{1.81}S NRs were synthesized via the hot injection method. In a typical synthesis of Cu_{1.81}S NRs having an aspect ratio of 4.8 (length vs. diameter), 6 mmol (ca. 1.45 g) of Cu(NO₃)₂·3H₂O, 42 mmol (ca. 10.6 g) of ODE, and 30 mmol (ca. 11.60 g) of TOPO-M were mixed in a 100-mL three-neck round bottom flask equipped with a thermocouple, a condenser, gas flow adapters, and a magnetic stir bar. The reaction system was then connected to the Schlenk line and placed in an oil bath. To form a homogeneous blue precursor, the mixture was heated to 80 °C under vacuum and maintained for 30 min. After that, Ar was blown into the flask with a flow rate of 100 mL·min⁻¹, providing an inert gas atmosphere for further reaction. Whereafter, the precursor was heated to 180 °C and kept for 30 min to remove gaseous by-products with low boiling points. Subsequently, under Ar blanket protection,

the flask was cooled to 80 °C by removing the oil bath. When the temperature reached 80 °C, 108 mmol (ca. 21.86 g) of *t*-DDT was injected into the flask by a 50-mL polypropylene syringe. Then, the flask was quickly placed in the oil bath and heated to 180 °C in 5 min. Upon reaching 180 °C, the solution changed from transparent yellow to brown in 2 min. And the solution became turbid after further reaction at this temperature, indicating the formation of NRs. The reaction was allowed to proceed for 15 min at 180 °C before being stopped by an ice water bath. When the flask temperature fell to 60 °C, 10 mL of *n*-hexane was added to the flask to prevent the solution from solidification and gelation. The resulted solution was transferred to 50-mL conical polypropylene centrifuge tubes. The product was precipitated by adding a 30-mL mixture of *n*-hexane and ethanol (with a volume ratio of 1:3) to each centrifuge tube, followed by centrifugation (8000 rpm, 5 min) and resuspension in *n*-hexane (10 mL). The above-outlined precipitation/centrifugation process was repeated three times before the NRs were dispersed in 5 mL of *n*-hexane. For the synthesis of Cu_{1.81}S NRs with an aspect ratio of 2.1, the synthetic parameters and operation conditions were similar as outlined above, except that 30 mmol of TOPO-M was replaced by 32 mmol (ca. 12.37 g) of TOPO-A.

2.3. Synthesis of CdS-Cu_{1.81}S HNRs and CdS NRs

The CdS-Cu_{1.81}S HNRs and CdS NRs were synthesized by cation exchange reaction using stock solutions with various Cd²⁺ contents [40]. All stock solutions were prepared using the same protocol. Prior to preparing the stock solution, the CdCl₂ powder was dried under a vacuum at 60 °C for 24 h to remove moisture entrained in the reagent. A certain amount of dried CdCl₂ powder, 24 mmol (ca. 6.42 g) of OLAM, and 30 mmol (ca. 7.57 g) of ODE were mixed in a 100-mL three-neck round bottom flask equipped with a thermocouple, a condenser, gas flow adapters, and a magnetic stir bar. The flask was connected to the Schlenk line and cycled with Ar and vacuum three times at room temperature. Then, the flask was placed under vacuum and heated to 80 °C. After the maintenance at 80 °C for 30 min, the flask was further heated to 200 °C under Ar flow (100 mL·min⁻¹) and held at this temperature for another 30 min, obtaining a homogeneous cation exchange stock solution (Cd-OLAM precursor). The stock solution was then cooled to the cation exchange temperature (ca. 105 °C). At the same time, 0.5 mmol (ca. 74 mg) of Cu_{1.81}S NRs, 4 mmol (ca. 1.49 g) of TOP, and 15 mmol (ca. 3.79 g) of ODE were mixed in a glass vial. The glass vial was sealed with a rubber septum under Ar protection. To form a colloidal suspension, the glass vial was sonicated for 10 min at room temperature. Subsequently, the obtained homogeneous Cu_{1.81}S NRs suspension was injected into the flask containing the cation exchange solution at 105 °C. After a 15-minute reaction at 105 °C, the flask was heated to 140 °C and held at this temperature for another 5 min before terminating the reaction by quenching in an ice water bath. The resulted product was isolated from the solution by the precipitation/centrifugation process. The detailed synthetic parameters of the CdS-Cu_{1.81}S HNRs and CdS NRs were listed in Table S1.

2.4. Sample characterizations

The transmission electron microscopy (TEM) images, high-resolution TEM (HRTEM) images, high angle annular dark-field scanning TEM (HAADF-STEM) images, and STEM energy-dispersive X-ray spectroscopy (STEM-EDS) maps were collected on an FEI Talos F200X S/TEM equipped with a Super-X detection system. The accelerating voltage for TEM and HRTEM images collection was 200 kV. The beam current for HAADF-STEM images and STEM-EDS maps collection was in the range of 0.15–0.75 nA. Cu Kα line, Cd L line, and S Kα line were used to label the corresponding elements in the EDS maps. All samples for TEM characterizations were prepared by the drop-casting technique. Typically, 10 μL of nanoparticles/*n*-hexane suspension was dropped onto 400-mesh molybdenum (Mo) grid with carbon/formvar film, and the

sample was dried in the air naturally. The dried powder samples were used for the powder X-ray diffraction (XRD) and X-ray photoelectron spectroscopy (XPS) measurements. The samples were isolated by the standard centrifugation/precipitation procedure from the nanoparticle/*n*-hexane suspension with a nanoparticle concentration of 100 mg·mL⁻¹. Then, the mud-like samples were dried in a vacuum at room temperature for 48 h, obtaining solid samples. The XRD patterns were recorded on a Bruker D8 Advance X-ray diffractometer using Cu K α radiation (λ = 0.15418 nm). The XPS spectra were recorded on a Thermo Scientific ESCALAB Xi X-ray photoelectron spectrometer. The samples dispersed in *n*-hexane were used directly for the optical absorption measurement. The absorption spectra of the samples were collected on a Shimadzu UV-1800 spectrophotometer.

2.5. Ligand exchange of the NRs and HNRs for photocatalytic HER

The photocatalysts synthesized using hot injection or cation exchange reaction were hydrophobic. To alter the hydrophilicity of the photocatalysts, MPA was decorated on the surface of the NRs and HNRs via ligand exchange reaction [17,41]. In brief, 200 mg of NRs or HNRs dispersed in 2 mL of *n*-hexane were isolated by the precipitate/centrifugation process. The resulted mud-like NRs or HNRs were dried under vacuum at room temperature for 24 h. The mildly dried NRs and HNRs were then transferred to a glass vial and sealed with a rubber septum under Ar protection. Subsequently, 20 mL of FMM solution containing 6% (volume fraction) of MPA was injected into the glass vial. The glass vial was sonicated at room temperature for 20 min, and a homogeneous suspension was formed. The nanocrystal suspension was further stirred for another 10 h, resulting in MPA decorated NRs or HNRs. The NRs or HNRs were washed twice with deionized water to remove excess FMM and MPA. The resulted hydrophilic NRs or HNRs were dried and stored under vacuum for further use and characterizations.

2.6. Photocatalytic hydrogen production

An all-glass automatic online trace gas analysis system (Labsolar-6A, Beijing Perfectlight) was adopted to investigate the photocatalytic hydrogen production performance of the NRs and HNRs. Typically, 20 mg of the as-synthesized photocatalyst was added to 100 mL of deionized water containing Na₂SO₃ (0.1 M) and Na₂S·9H₂O (0.1 M), and the mixture was sealed in a closed-gas circulation system. The reaction system was cycled with Ar and vacuum five times to remove the dissolved air before irradiation. The reaction cell was placed in a cryogenic circulating water bath with a constant temperature of 5 ± 0.2 °C, and a 300 W Xenon lamp source (PLS-SXE300D, Beijing Perfectlight) was used to simulate the solar irradiation. The light intensity at the sample position was 100 ± 10 mW·cm⁻² measured by a radiation meter (PL-MW2000, Beijing Perfectlight). The amount of H₂ was determined using gas chromatography (GC 9790II, thermal conductivity detector, TCD, Ar carrier, Fuli Instruments). In the stability test, an additional 1 mmol Na₂S·9 H₂O and Na₂SO₃ were added after each cycle to avoid photo-corrosion of the catalyst caused by the reduction of sacrifice agents and then evacuated the sealed vessel for half an hour.

The apparent quantum efficiency (AQE) of the optimized CdS-Cu_{1.81}S HNRs was measure using the same setup parameters and operating conditions except that the 420 nm (± 10 nm) band-pass filter was used to limit the irradiation band of the simulated solar light. The average irradiation intensity was determined to be 2.52 mW·cm⁻² by the radiation meter. The AQE was calculated by the following equation [41]:

$$\text{AQE}(\%) = \frac{\text{number of evolved hydrogen molecules} \times 2}{\text{number of incident photons}} \times 100\%$$

2.7. Photoelectrochemical (PEC) measurements

A standard three-electrode system was used to measure the photoelectrochemical properties of the photocatalysts. The working electrode was prepared by spin-coating the photocatalyst onto a 1 × 1 cm² FTO glass. Before use, the working electrode was dried in a vacuum at 60 °C for an hour. A 1 × 1 cm² platinum (Pt) sheet was used as the counter electrode. An Ag/AgCl electrode in a 3 M KCl solution was used as the reference electrode. A 0.1 M Na₂SO₄ solution was used as the electrolyte.

The PEC measurements were performed on an electrochemical workstation analysis platform (Autolab PGSTAT302N and impedance analyzer μStat-i 400, Metrohm) under a 300 W Xenon lamp irradiation (SS-F5-3A, Enlitech). The transient photocurrent-time curves with the light on/off cycles measurements were recorded under a bias voltage of -0.4 V vs. Ag/AgCl. Under dark, the electrochemical impedance spectra (EIS) were recorded on the impedance analyzer in the frequency range of 10⁵ to 10⁻¹ Hz with an AC amplitude of 10 mV. The Mott-Schottky plots were measured on the impedance analyzer at 10³ Hz without irradiation. The measured potentials vs. Ag/AgCl electrodes were converted to those vs. normal hydrogen electrodes (NHE) according to the previous report (i.e. E_{NHE} = E_{Ag/AgCl} + 0.197) [22].

2.8. Carrier dynamics measurements

The femtosecond time-resolved pump-probe technique was employed to investigate the interface charge dynamics. The laser pulse was produced by an optical parametric amplifier (TOPAS, USF-UV2), pumped by a Ti: sapphire regenerative amplifier system (Spectra-Physics, Spitfire ACE-35 F-2KXP, Maitai SP and Empower 30). The pulse repetition rate was 2 kHz with a pulse duration of 35 fs. The pump and probe light was focused on the sample by a lens with a focal distance of 150 mm and the minimum beam waist was approximately 38 mm. All the samples were dispersed in NMP for this test.

3. Results and discussion

3.1. Characterizations of Cu_{1.81}S NRs, CdS-Cu_{1.81}S HNRs, and CdS NRs

As sketched in Fig. 1a, roxbyite Cu_{1.81}S NRs with hexagonal tips were initially prepared as parent nanocrystals. Then, by mixing 0.25 mmol of Cd²⁺ precursor with 0.50 mmol of template Cu_{1.81}S NRs suspension, CdS-Cu_{1.81}S HNRs were obtained through a stoichiometrically limited cation exchange reaction [40]. In the presence of excess Cd²⁺ precursor, almost all the Cu cations were replaced by Cd²⁺, resulting in onefold CdS NRs formation. Fig. 1b reveals the uniform and well-defined Cu_{1.81}S NRs depositing on the molybdenum grid in standing-up and level fashions. The lattice spacing of 0.335 nm measured from the image of a high-resolution transmission electron microscopy (HRTEM) corresponds to (100) planes of roxbyite Cu_{1.81}S (Fig. 1c). High-angle annular dark-field scanning TEM (HAADF-STEM) image and STEM energy-dispersive X-ray spectroscopy (STEM-EDS) element maps confirm the corresponding relation between composition and morphology of Cu_{1.81}S NRs (Fig. 1d and e). The average length of Cu_{1.81}S NRs is calculated to be 87.6 ± 11.8 nm with an aspect ratio (AR) of 4.8 (Fig. 1f). When we replaced a fraction of Cu⁺ in the parent Cu_{1.81}S NRs with Cd²⁺ by cation exchange reaction, the shapes and sizes of the obtained HNRs remain unchanged (Fig. 1g and k). HRTEM image presents a newly engineered internal interface between material components (Fig. 1h). Two definite lattice fringes, corresponding to (100) planes of roxbyite Cu_{1.81}S (0.335 nm) and (002) planes of greenockite CdS (0.336 nm), are intimately integrated on a single nanorod. STEM-EDS element maps show the HNRs have a distinct segmentation pattern (Fig. 1i and j). Results corroborate the products generated from the stoichiometrically limited cation exchange reaction are two-component HNRs with discrete Cu_{1.81}S and CdS domains. Further, to synthesize

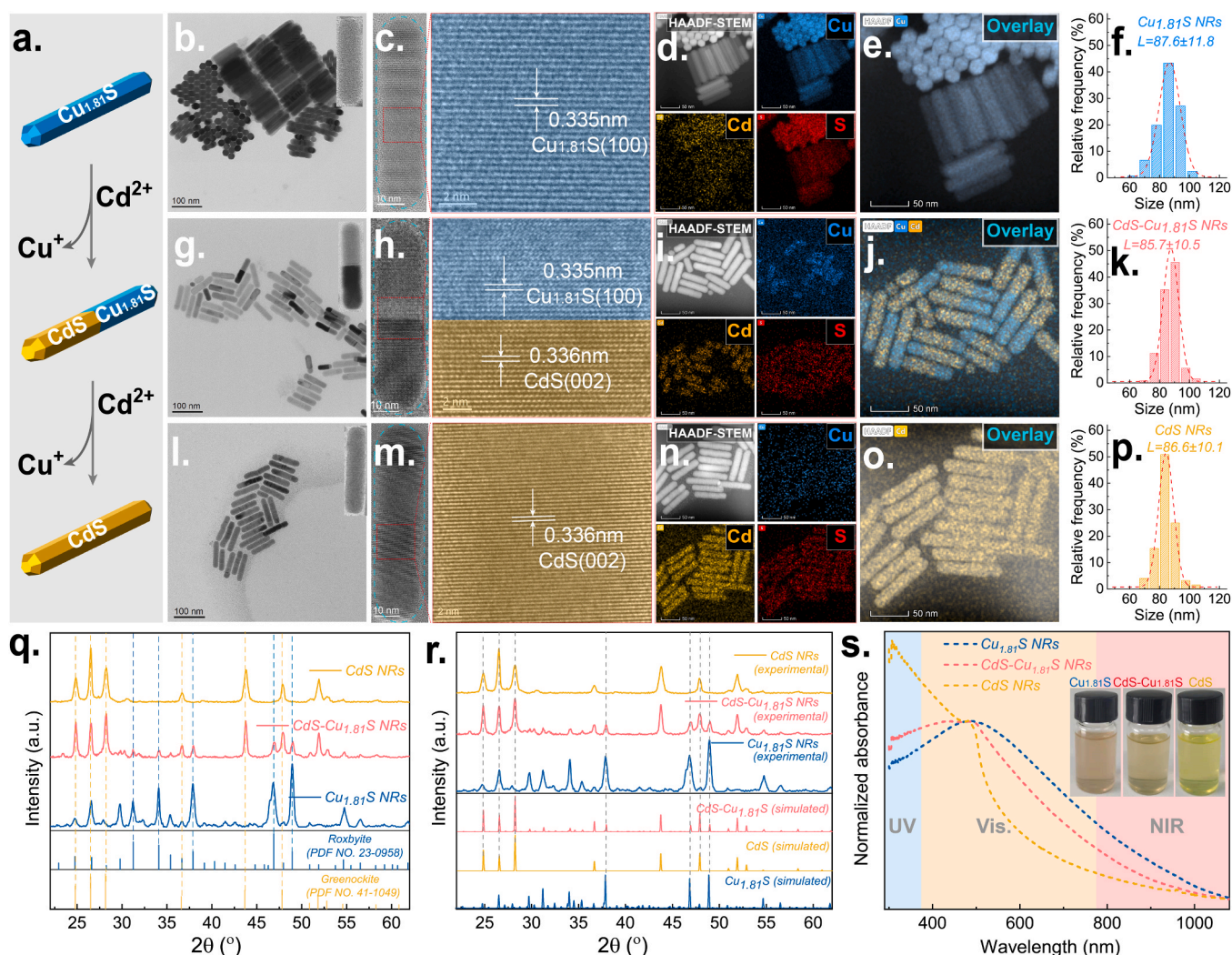


Fig. 1. Formation of the HNRs. Schematic shows the formations of $\text{CdS-Cu}_{1.81}\text{S}$ HNRs and CdS NRs from the $\text{Cu}_{1.81}\text{S}$ template NRs by cation exchange reactions (a). TEM images of $\text{Cu}_{1.81}\text{S}$ NRs, $\text{CdS-Cu}_{1.81}\text{S}$ HNRs, and CdS NRs (b, g, and l). HRTEM images for $\text{Cu}_{1.81}\text{S}$ NRs, $\text{CdS-Cu}_{1.81}\text{S}$ HNRs, and CdS NRs (c, h, and m). HAADF-STEM images and corresponding EDS maps for $\text{Cu}_{1.81}\text{S}$ NRs, $\text{CdS-Cu}_{1.81}\text{S}$ HNRs, and CdS NRs (d, i, and n). Merged images of HAADF-STEM and EDS maps for $\text{Cu}_{1.81}\text{S}$ NRs, $\text{CdS-Cu}_{1.81}\text{S}$ HNRs, and CdS NRs (e, j, and o). Average length histograms of $\text{Cu}_{1.81}\text{S}$ NRs, $\text{CdS-Cu}_{1.81}\text{S}$ HNRs, and CdS NRs (f, k, and p). Powder XRD patterns of the NRs in contrast with standard PDF cards (q) and simulated patterns (r). UV-vis-NIR absorption spectra and digital photographs (insets) of the NRs dispersed in *n*-hexane (s).

pure phase CdS NRs, we introduced excess Cd^{2+} precursor to the cation exchange reaction. As expected, the shapes and sizes of the resulted CdS NRs inherit from the parent $\text{Cu}_{1.81}\text{S}$ NRs (Fig. 1l and p). HRTEM image STEM-EDS element maps confirm the CdS NRs are monocomponent in single-crystal form as no Cu signal can be observed beyond the background level (Fig. 1m-o).

Apart from the composition and morphology, we examined the crystallographic structures and optical absorption properties of the NRs. Powder X-ray diffraction (XRD) peaks of parent copper sulfide NRs can be indexed to roxbyite $\text{Cu}_{1.81}\text{S}$ (JCPDS no. 23-0958), whereas the XRD peaks of cadmium sulfide NRs agree with those of greenockite CdS (JCPDS no. 41-1049). The XRD pattern of heterogeneous NRs presents characteristic diffraction peaks of both roxbyite $\text{Cu}_{1.81}\text{S}$ and greenockite CdS , revealing the existence of two different phases in the HNRs (Fig. 1q). A more accurate comparison was performed to further identify the occurrence states of copper sulfide and cadmium sulfide using simulated XRD patterns. Simulated XRD patterns were generated by Bragg's equation according to the standard crystallographic information [42-44]. By combining 50% of the roxbyite phase $\text{Cu}_{1.81}\text{S}$ and 50% of the greenockite phase CdS , a simulated XRD pattern of immiscible $\text{CdS-Cu}_{1.81}\text{S}$ crystal phases was engendered. As shown in Fig. 1r, the

characteristic XRD peaks of the experimental $\text{CdS-Cu}_{1.81}\text{S}$ pattern matches well with those of the simulated pattern, and no 2θ shift can be observed. From the opposite point, if Cd^{2+} dopes in the $\text{Cu}_{1.81}\text{S}$ lattice and forms $\text{Cd}_x\text{Cu}_{1.81-2x}\text{S}$ alloy phase, according to Vegard's law, obvious 2θ shifts should be detected as the lattice constants change [45]. The evidence indicates the two components in the HNRs form separate domains.

Fig. 1s shows the UV-vis absorption spectra of the NRs. CdS NRs give a strong near-ultraviolet absorption (300–500 nm). And $\text{Cu}_{1.81}\text{S}$ NRs possess a broad UV-vis-NIR absorption between 400 and 1000 nm. Previous reports indicate the NIR absorption of copper sulfide can be extended to 2300 nm, owing to the localized surface plasmon resonance [46]. According to Tauc plots, the measured bandgaps of CdS and $\text{Cu}_{1.81}\text{S}$ NRs are 2.32 eV and 1.69 eV, respectively (Fig. S1), which roughly define their light absorption bands. For $\text{CdS-Cu}_{1.81}\text{S}$ HNRs, the optical absorption is enhanced at both ultraviolet and visible light regions. That is because the light absorption of $\text{Cu}_{1.81}\text{S}$ and CdS compensate for each other when combining them on a single nanorod. Due to its broadband absorption, $\text{CdS-Cu}_{1.81}\text{S}$ HNRs can be used as an excellent light-harvesting material.

In addition, X-ray photoelectron spectroscopy (XPS) was further

performed to analyze the elemental composition and chemical state of the samples, as shown in Fig. 2. The overall survey spectra describe the presence of sulfur and carbon and also depict the compositional evolutions of cadmium and copper along with the cation exchange reaction. The high-resolution scanning results of Cu 2p, Cd 3d, and S 2p are shown in Fig. 2b-d. The binding energy peaks of Cu 2p are located at 932.4 eV and 952.3 eV, representing Cu 2p_{3/2} and Cu 2p_{1/2} of Cu_{1.81}S, respectively. The peaks of Cu 2p shift to lower energy positions ($\Delta E_{\text{Cu 2p}}$ (after-before) ≈ -0.9 eV) after partial cation exchange reaction. This difference attributes to the change in the chemical environment of the copper atoms at the heterointerface, that is Cu-S-Cu bonds in Cu_{1.81}S NRs transform into Cu-S-Cd bonds in CdS-Cu_{1.81}S HNRs after partial cation exchange reaction. Besides, no “shake-up” peak is found in the high-resolution spectra of Cu 2p, which confirms the chemical status of Cu is Cu⁰ or Cu(I). Further, the Auger peaks of Cu are observed at 568.7 eV in the Cu LMM spectra (Fig. 2b inset), indicating the only existence of Cu (I) [47]. The Cu 2p peaks are disappeared after the complete cation exchange from Cu_{1.81}S to CdS. In the meantime, two strong peaks, locating at 405.1 eV and 411.8 eV, are observed after partial and complete cation exchange reactions, corresponding to Cd 3d_{5/2} and Cd 3d_{3/2}, respectively. It demonstrates that the Cd element exists in the form of Cd (II) in both CdS-Cu_{1.81}S HNRs and CdS NRs [22]. Fig. 2d shows the peaks of S 2p_{3/2} and S 2p_{1/2} are located at 161.6 eV and 162.8 eV, respectively, indicating the chemical state of S is -2 [48]. Notably, the peaks of S 2p shift to lower positions after cation exchange, suggesting the chemical environment of S atoms gradually changes from Cu-S-Cu to Cu-S-Cd and Cd-S-Cd. Since the binding energy change of S 2p is small (ca. 0.40 eV), the valence of S is maintained during the cation exchange reaction. In addition, Gaussian fitting results show both S 2p_{3/2} and S 2p_{1/2} split into two distinct peaks around 161.57 eV and 162.77 eV, respectively,

indicating that there are two different chemical states (Cu-S and Cd-S) of S element in CdS-Cu_{1.81}S HNRs. On the other hand, the binding energies of Cu 2p, Cd 3d, and S 2p of CdS-Cu_{1.81}S HNRs are shifted compared to those of onefold Cu_{1.81}S and CdS NRs, demonstrating that the electron interaction between the two domains of Cu_{1.81}S and CdS in HNRs is enhanced [49,50].

3.2. Features of the heterointerfaces in CdS-Cu_{1.81}S HNRs

To further characterize the interfaces in CdS-Cu_{1.81}S HNRs, we obtained the HRTEM image of the heterointerface and compared the results to the standard crystal structures. A highly crystalline and defect-free heterointerface can be observed in Fig. 3a. The (002) plane of CdS coherently attaches to the (100) plane of Cu_{1.81}S. The atom arrangement from the HRTEM image matches well with that from the simulated heterointerface pattern (Fig. 3b). Greenockite CdS, formed via cation exchange, has a hexagonal closed-packed (*hcp*) S sublattice, and the lattice constants of 6.714 Å and 4.137 Å correspond to *a* and *c*, respectively. Whereas, the parent roxbyite Cu_{1.81}S crystal possesses a distorted *hcp* S sublattice. Such a pseudohexagonal wurtzite-like subcell of roxbyite Cu_{1.81}S can be directly used for comparison with that of CdS. The average *a* and *c* of the pseudohexagonal Cu_{1.81}S subcell are 6.703 Å and 3.887 Å, respectively. These lattice parameters allow for a convenient comparison of crystallographic information to qualitatively predict rational heterointerface forms. Fig. 3c shows three heterointerface forms, which have the best lattice matching and less strain. Detailed calculation results indicate the lattice mismatches at *a*-*a*, *c*-*c*, and angled (ca. 40°) directions are 0.16%, 6.04%, and 3.49%, respectively (Table S2). Such small lattice mismatches suggest low interface stress, fewer dislocation defect, and excellent structural continuity in the

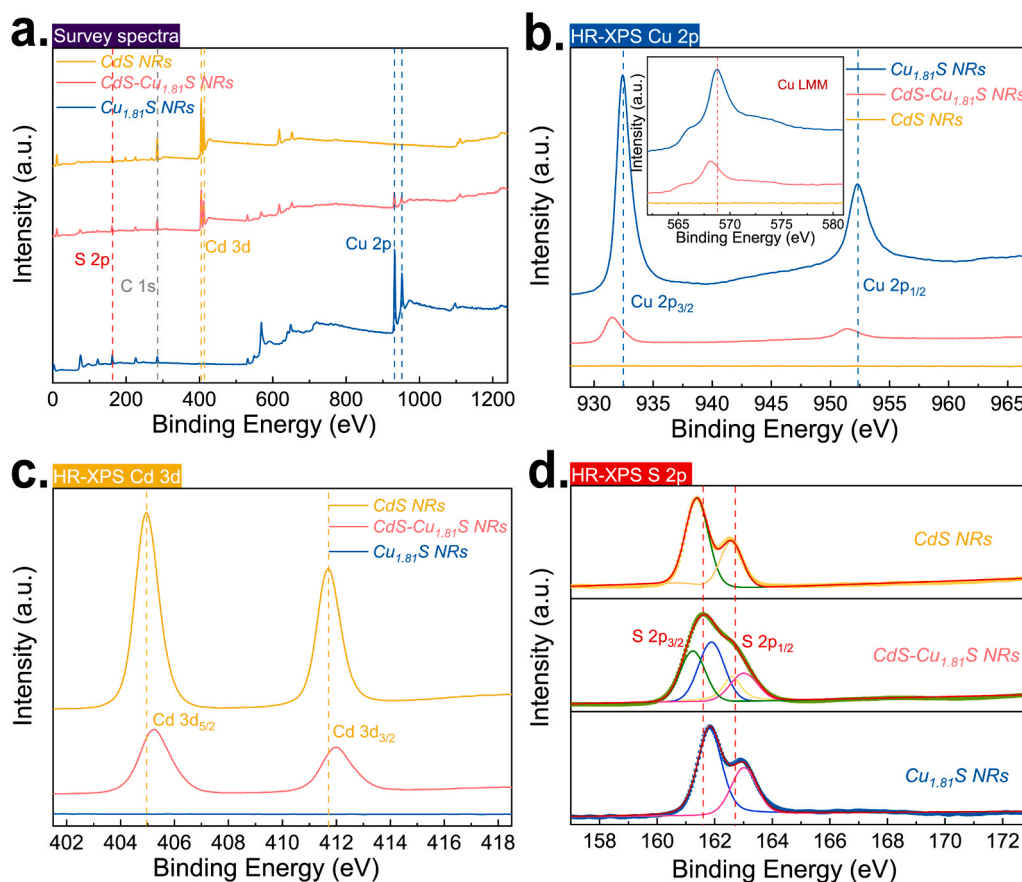


Fig. 2. Chemical status of the elements. (a) XPS survey spectra. (b-d) High-resolution XPS spectra (HR-XPS) of Cu 2p, Cd 2p, and S 2p, respectively. The inset of (b) is the Auger Cu LMM spectra.

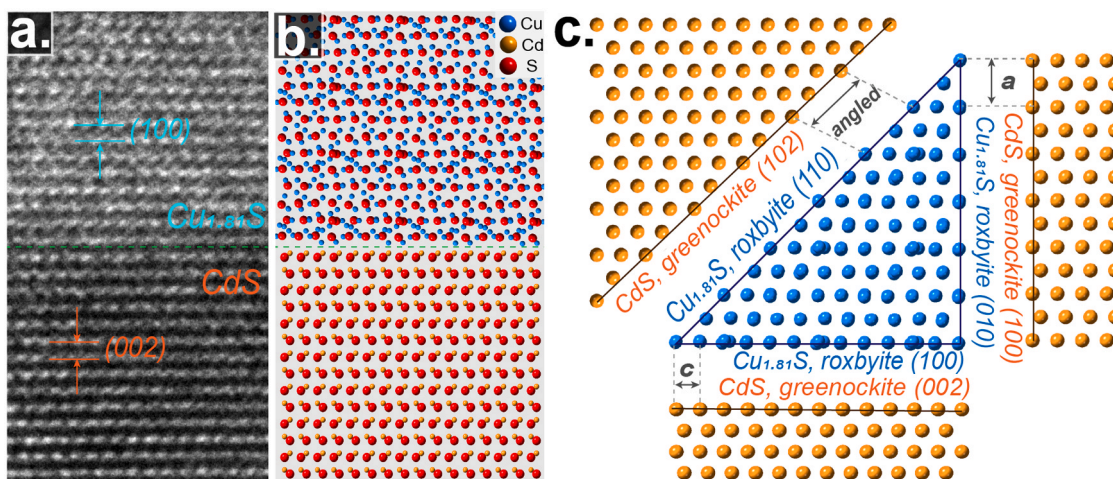


Fig. 3. Interface structure of the HNRs. HRTEM image of the $\text{CdS-Cu}_{1.81}\text{S}$ heterointerface (a). Perfect $\text{CdS-Cu}_{1.81}\text{S}$ heterointerface structure from simulation (b). Idealized projections of the crystal planes of sulfur sublattice between roxbyite $\text{Cu}_{1.81}\text{S}$ and greenockite CdS (c).

HNRs. And all these factors play essential roles in regulating the charge transfer and recombination at the heterointerfaces. Therefore, high-quality interfaces, built by cation exchange, in $\text{CdS-Cu}_{1.81}\text{S}$ HNRs are in favor of efficient charge transfer and contribute to lessening electron-hole recombination centers theoretically.

3.3. Photocatalytic Activity of $\text{CdS-Cu}_{1.81}\text{S}$ HNRs in HER

In addition, we employed Mott-Shottky measurements to qualitatively determine the semiconductor types and to estimate the band structures of the NRs. Fig. S2 shows the Mott-Shottky (M-S) plots of $\text{Cu}_{1.81}\text{S}$, CdS , and $\text{CdS-Cu}_{1.81}\text{S}$ NRs. Results indicate $\text{Cu}_{1.81}\text{S}$ is a *p*-type semiconductor as its tangent slope is negative, whereas the tangent slope of CdS is positive, revealing its *n*-type character. Demonstrating the

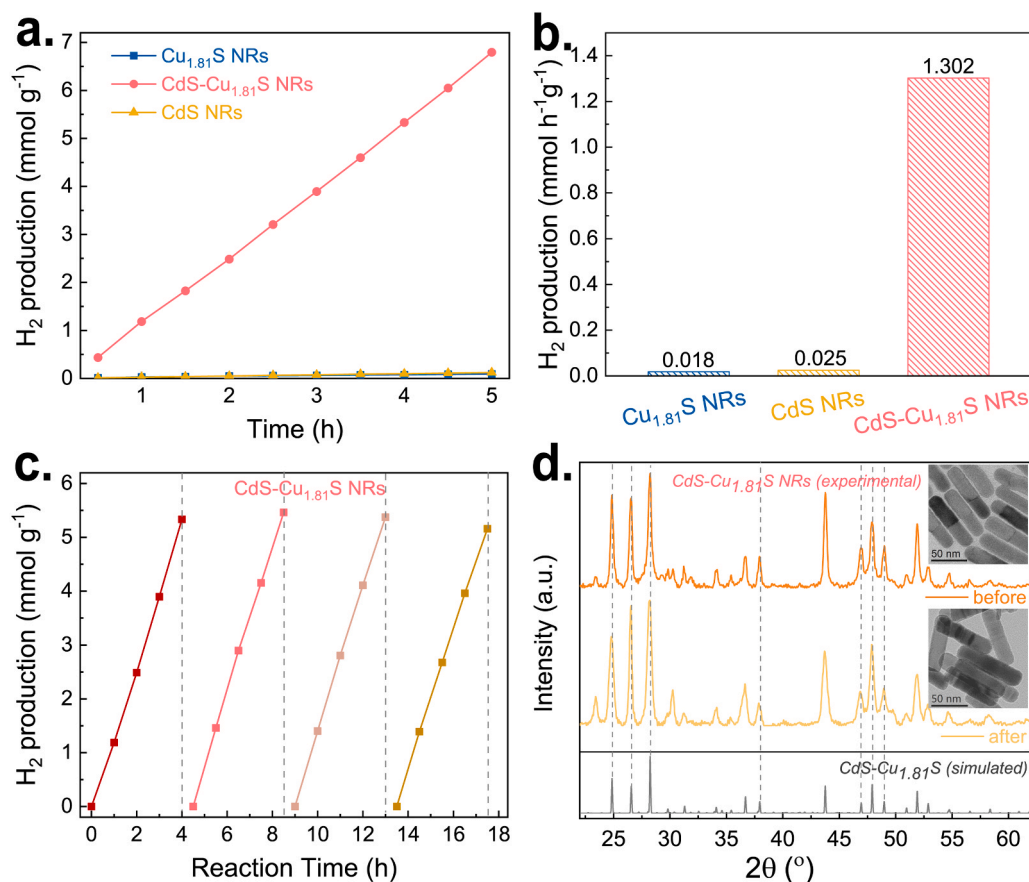


Fig. 4. Photocatalytic hydrogen evolution reaction (HER). (a) H_2 production under simulated solar irradiation (Intensity: 100 mW cm^{-2}) using different NRs as the photocatalysts. (b) Corresponding hydrogen production rates of the NRs. (c) Stability test of $\text{CdS-Cu}_{1.81}\text{S}$ HNRs (the reaction system was evacuated for 30 min every 4 h). (d) Powder XRD patterns and TEM images (insets) of $\text{CdS-Cu}_{1.81}\text{S}$ HNRs before and after the photocatalytic reaction.

formation of *p-n* junction in the CdS-Cu_{1.81}S system. Combining with the Tauc plots, the electronic band structures of the NRs can be estimated. The edge potentials of Cu_{1.81}S, CdS, and CdS-Cu_{1.81}S NRs are -1.03 , -0.70 , and -0.55 V (vs. $E_{\text{Ag/AgCl}}$ at pH 7, NHE), respectively. Attributing to the strong interaction between Cu_{1.81}S and CdS, the edge potential of CdS-Cu_{1.81}S NRs is more positive than that of CdS, which is closer to the redox potential of H^+/H_2 (-0.42 V vs. NHE at pH 7) [22,51, 52]. And the edge potential of a photocatalyst is essential for H^+ reduction.

The above fully demonstrates the CdS-Cu_{1.81}S HNRs have the properties of broadband absorption, a high degree of crystallinity, neat interfaces at the atomic level, precisely adjusted edge potentials, and a built-in electronic field. And these intrinsic physical characteristics conform to the design principles of an ideal photocatalyst as outlined before. Thus, exploiting their benefits of the synergetic absorption, high crystallinity, fine interface, and tailored energy band, the CdS-Cu_{1.81}S HNRs were employed for photocatalytic H_2 production. The photocatalytic activity of CdS-Cu_{1.81}S HNRs was evaluated using 100 mL of deionized water containing 0.1 M Na_2SO_3 and 0.1 M Na_2S as sacrifice agents under 100 mW cm^{-2} of simulated solar light irradiation. For comparison, the photocatalytic performances of pristine Cu_{1.81}S NRs and onefold CdS NRs were also examined under identical reaction conditions. Results indicate superior activity of CdS-Cu_{1.81}S HNRs, achieving an H_2 production rate of $1.302 \text{ mmol} \cdot \text{h}^{-1} \cdot \text{g}^{-1}$. It is approximately 72 and 52 times higher than those of pristine Cu_{1.81}S NRs and onefold CdS NRs, respectively (Fig. 4a, b, and Fig. S3). These results also reinforce the point that broadband absorption, high-quality heterointerface, and built-in electronic field are favorable for charge generation, separation, and transport. The stability of the heterogeneous

photocatalyst was tested by monitoring the H_2 production under continuous reaction. As shown in Fig. 4c, the H_2 production rate of CdS-Cu_{1.81}S HNRs maintains fairly constant during four cycles reaction. In the continuous reaction, there is only a 5.56% difference between the maximum and minimum H_2 production rates (Table S3). We further investigated the morphology and crystal structure changes of the CdS-Cu_{1.81}S HNRs after the photocatalytic reaction. The TEM image and XRD pattern demonstrate, after long-term and continuous reaction, the CdS-Cu_{1.81}S HNRs remain monodisperse, well-defined, and highly crystalline (Fig. 4d). Such excellent stability of the CdS-Cu_{1.81}S HNRs attributes to the continuous anion sublattice and defect-free heterointerface, which provide a steady crystal framework for resisting photocorrosion.

3.4. Mechanism for photocatalytic HER

To clarify the charge separation, transport, and electron-hole recombination in the NRs, photo electrochemistry experiments were carried out [53]. The Nyquist diagrams and the transient photocurrent responses of the NRs were obtained with on/off cycles of visible light irradiation. As illustrated in Fig. 5a, the semicircle radius of CdS-Cu_{1.81}S HNRs is smaller than that of CdS NRs. It suggests the charge transport resistance in CdS-Cu_{1.81}S HNRs is small, implying a promoted charge separation and a fast carrier transfer. Results of the transient photocurrent responses show the CdS-Cu_{1.81}S HNRs possess the largest photocurrent, indicating the electron-hole recombination in CdS-Cu_{1.81}S HNRs is low (Fig. 5b). Fig. 5c depicts the charge transfer mechanism of the CdS-Cu_{1.81}S HNRs photocatalytic system [54].

The carrier dynamics of the heterostructured photocatalysts were explored using the femtosecond time-resolved pump-probe technique

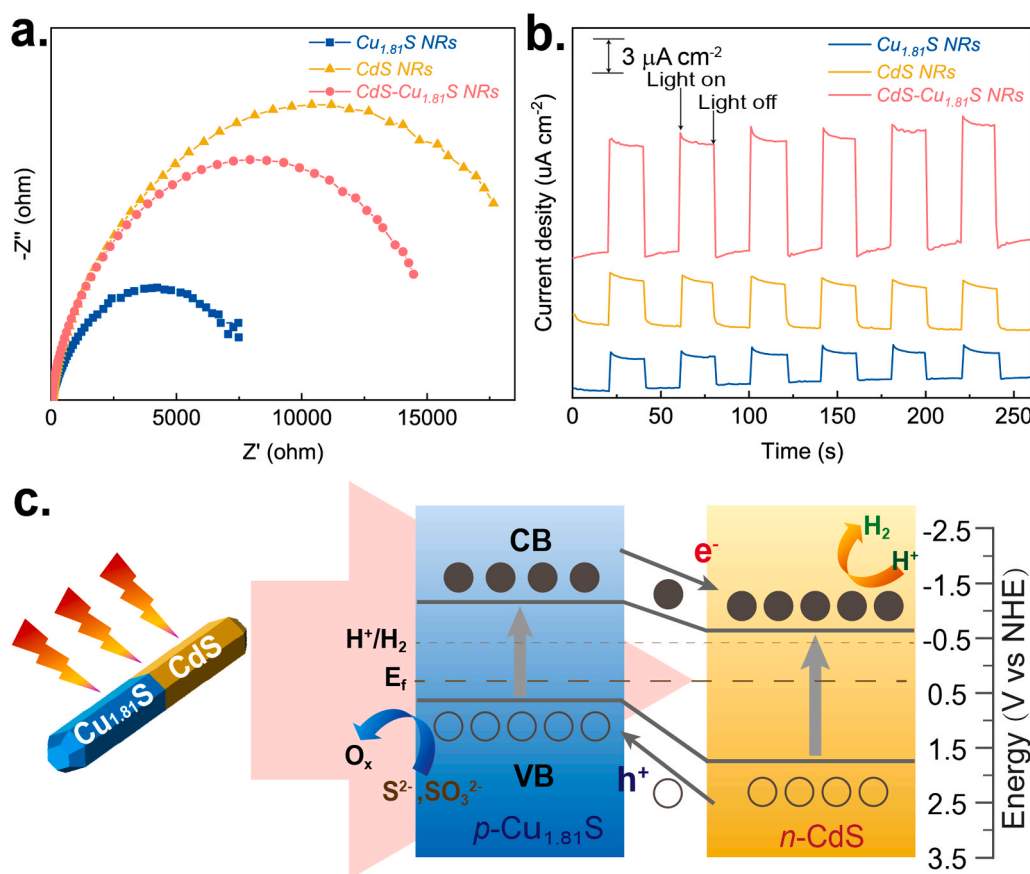


Fig. 5. Photoelectrochemical (PEC) measurements and mechanisms. (a) Nyquist plots of the NRs under a dark environment. (b) Transient photocurrent responses of the NRs (irradiation was switched at the bias of -0.4 V vs. Ag/AgCl , and the time interval was 20 s). (c) Schematic shows the charge transfer mechanism of the HER using CdS-Cu_{1.81}S HNRs as the photocatalyst (CB: conduction band, VB: valence band, and E_f : Fermi level).

[55,56]. The carrier dynamics relaxation processes for all samples were obtained at the pump and probe wavelengths of 400 nm. The pump incident intensity was 200 nJ, which is below the excitation intensity of the solvent. All transient signals clearly show exponential decay. A biexponential decay model, $y = A_1 \exp(-t/\tau_1) + A_2 \exp(-t/\tau_2)$, is employed to fit these recorded signals, as shown in Fig. S4. The values of τ_1 and τ_2 for Cu_{1.81}S NRs, CdS NRs, and CdS-Cu_{1.81}S HNRs were 0.79 ps and 16.84 ps, 0.77 ps and 9.03 ps, and 0.62 ps and 23.35 ps, respectively. For Cu_{1.81}S NRs and CdS NRs, the faster decay time, usually at a subpicosecond level, represents the intraband relaxation process, while the slower decay time, usually at a picosecond level, corresponds to the trapping processes from the conduction band edge to shallow trap states [57,58]. Besides, a long tail was monitored in the pump-probe signal of Cu_{1.81}S NRs, indicating a longer electron lifetime. This process can be ascribed to the electron relaxation from the shallow trap state to the

deep trap state, which is usually at a nanosecond level [57]. For the CdS-Cu_{1.81}S HNRs, the profile is similar to that of CdS NRs. No tail was observed after 60 ps photoexcitation. Given the formation of the *p-n* junction between Cu_{1.81}S and CdS domains, electrons generated in Cu_{1.81}S by pump light excitation quickly migrate into the conduction band of CdS. Subsequently, the photoexcited electrons rapidly accumulated in the conduction band of CdS, which may accelerate the photogenerated electron dynamic intraband relaxation [55]. Thus, compared to that in CdS NRs, a relatively fast relaxation time of τ_1 can be observed in CdS-Cu_{1.81}S HNRs (0.62 ps vs. 0.77 ps). Moreover, the prolonged τ_2 observed in CdS-Cu_{1.81}S HNRs may be attributed to more shallow trap states in the heterostructured NRs, which is helpful for the improvement of photocatalytic H₂ production activity [59].

Electron excitation, electron-hole separation, and charge transfer are three of the most critical processes of the photocatalytic HER. A

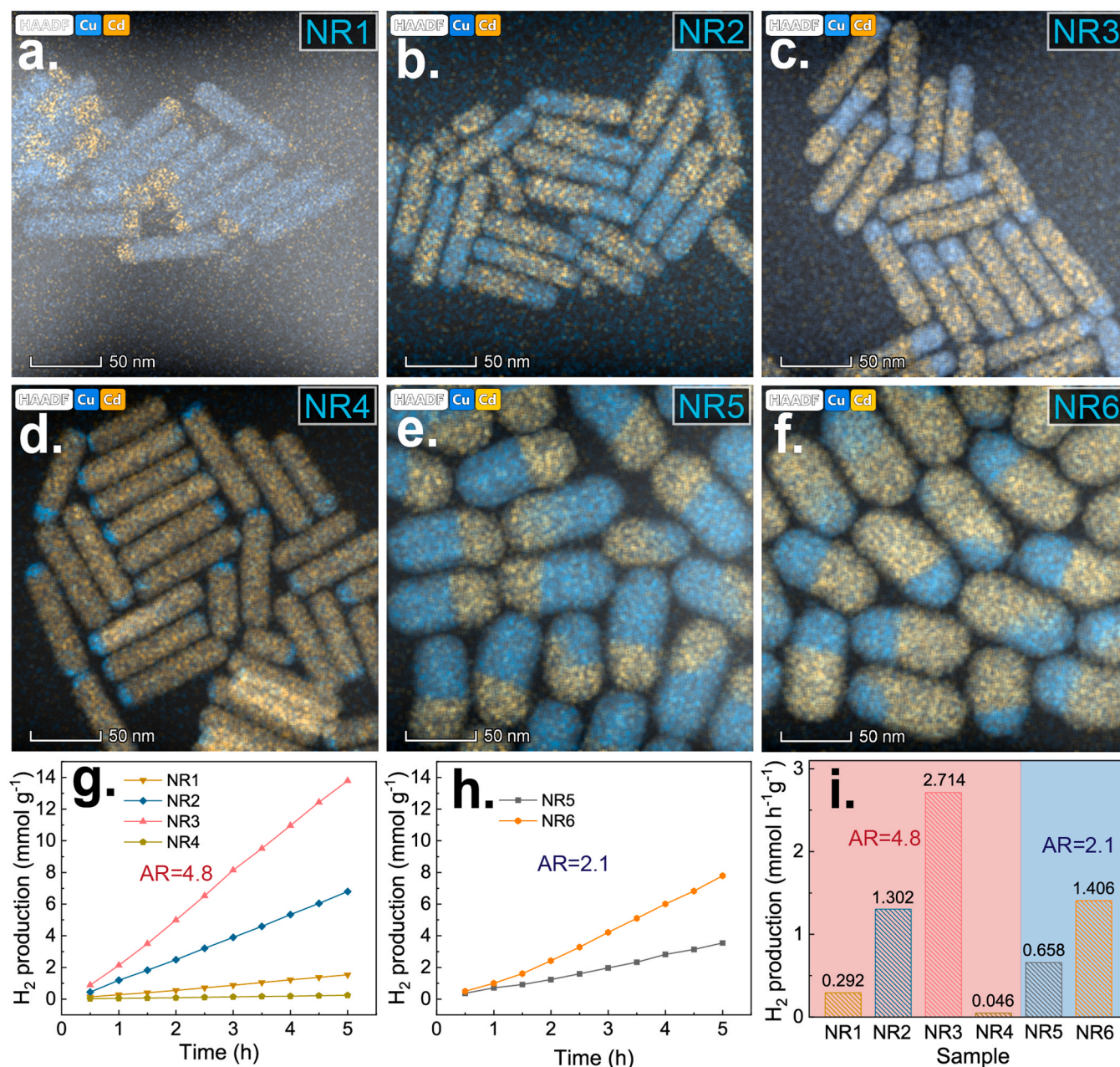


Fig. 6. Photocatalytic performance optimization of the CdS-Cu_{1.81}S HNRs. (a-f) Merged images of HAADF-STEM and STEM-EDS maps for CdS-Cu_{1.81}S HNRs with different CdS/Cu_{1.81}S ratios and various aspect ratios (a-d: AR=4.8, e-f: AR=2.1). (g-h) H₂ production under simulated solar light irradiation (Intensity: 100 mW cm⁻²) using NRs with different aspect ratios as the photocatalysts. (i) Comparison of photocatalytic H₂ production rates of the NRs.

recession of any of these processes may result in attenuated photocatalytic H_2 production efficiency, namely buckets effect. Although efforts have been made to promote the electron excitation and charge separation by epitaxially growing heterogeneous components on substrate crystals and internally constructing p - n junction, the ignorance of building high-quality heterointerface becomes the short stave that limits the efficiency improvement of H_2 production. And poor interface structure usually leads to high electron-hole recombination and severe photocorrosion and eventually results in insufficient H_2 production efficiency and low stability of the photocatalyst [60]. In this work, under the premise of ensuring the broadband absorption and the existence of internal p - n junction, high-quality heterointerfaces have been constructed in the CdS - $Cu_{1.81}S$ HNRs by cation exchange reaction, which brings integral improvement on H_2 production efficiency and photocatalyst durability.

3.5. Optimization of CdS - $Cu_{1.81}S$ HNRs for photocatalytic HER

Based on the above work, by finely tuning their shapes and domain compositions, we further optimized the photocatalytic performance of the CdS - $Cu_{1.81}S$ HNRs. Two types of $Cu_{1.81}S$ NRs, with aspect ratios (ARs) of 4.8 and 2.1 (Fig. S5), were used as the templates for the stoichiometrically limited cation exchange reaction. By varying the Cd^{2+} concentrations, six kinds of CdS - $Cu_{1.81}S$ HNRs with diverse domain compositions and ARs (marked as NR1-NR6) were obtained. HAADF-STEM and STEM-EDS merged images of the HNRs show the fraction of the CdS domain evolves proportionally with the ingoing cation dosage (Fig. 6a-f). Subsequently, the photocatalytic activities of the HNRs were evaluated, as shown in Fig. 6g-i. Results indicate the H_2 production efficiencies can be promoted with the increment of CdS fraction in both photocatalytic systems using the HNRs with the ARs of 4.8 and 2.1. When the CdS fractions are comparable, the H_2 production rates using AR 4.8-type HNRs are higher than those using AR 2.1-type HNRs. The H_2 production efficiency of NR3 achieves $2.714 \text{ mmol} \cdot \text{h}^{-1} \cdot \text{g}^{-1}$, which is 150 times and 108 times higher than those of pristine $Cu_{1.81}S$ NRs and onefold CdS NRs. The obtained apparent quantum efficiency (AQE) of NR3 at 420 nm is 11.32%, which is comparable to that of the noble metal-based photocatalyst [28,61]. Notably, when the fraction of the CdS domain is elevated to the level close to pure phase CdS , a dramatic drop in H_2 production is observed. HER from water splitting occurs at the surface reduction sites of the photocatalyst [62]. Thus, more surface reaction sites signify promoted kinetics of redox reactions. Moreover, the equilibrium between the H^+ reduction and hole elimination reactions also controls the H_2 production efficiency. Slower reaction kinetics of hole elimination may result in hole accumulation at the oxidation sites, which hinders electron-hole separation and encourages charge recombination. In our photocatalytic system, H^+ is reduced at the surface sites of CdS domains by photogenerated electrons, and the holes are scavenged by Na_2S/Na_2SO_3 couple at the surface sites of $Cu_{1.81}S$ domains. Therefore, increasing the fraction of CdS domains provides more H^+ reduction sites at the surface and further brings improved H_2 production efficiency (e.g. NR1 to NR3 and NR5 to NR6). As the surface area of AR 4.8-type HNRs is approximately 1.94 times larger than that of AR 2.1-type HNRs, more surface reaction sites contribute to the higher H_2 production efficiency of AR 4.8-type HNRs (e.g. NR2 vs. NR5 and NR3 vs. NR6). When the oxidation sites are scarce, the kinetically insufficient elimination of holes suppresses the photocatalytic hydrogen evolution, resulting in a low H_2 production rate (e.g. NR4). Consequently, to improve the performance of the photocatalyst, synergetic considerations on the number of active reaction sites and the kinetic equilibrium of redox reactions are also essential.

Besides, it is worth noting that, except for the factors outlined above, carrier diffusion distance and carrier injection mode seem to be potential factors that also contribute to the utilization of photogenerated carriers. As shown in Fig. 6c, we find about 21.6% of HNRs with double-tip structures (CdS - $Cu_{1.81}S$ - $Cu_{1.81}S$) mix in a large number of single-tip

ones (CdS - $Cu_{1.81}S$). The unique double-tip structure alters the carrier transport mode from one-way into two-way, which suggests a more effective carrier injection and a shorter diffusion distance. In theory, a short diffusion distance is in favor of the carrier hopping from the interior to the surface, which may promote the reaction kinetics. Although the evidence presented here is yet sufficient to verify the contribution of the double-tip structure on photocatalytic hydrogen evolution, it is a valuable entry point for improving the performance of the heterogeneous photocatalysts in the future.

4. Conclusion

In summary, we have synthesized a series of CdS - $Cu_{1.81}S$ HNRs with continuous sublattice structures and high-quality interfaces by stoichiometrically limited cation exchange reaction for photocatalytic HER. The precisely designed CdS - $Cu_{1.81}S$ HNRs integrate various advantages of broadband light-harvesting, efficient charge separation, less electron-hole recombination, suitable band edge potential, excellent stability, and low cost. We have also found considerations on reaction sites and redox reaction equilibrium are equally important for the photocatalytic performance improvement of the HNRs. The H_2 production efficiency of the synergetically designed CdS - $Cu_{1.81}S$ HNRs achieves further ascent by fine-tuning their aspect ratios and domain contents. Meanwhile, our work also broadens the application scope of the emerging nanoscale cation exchange reaction, which realizes the seamless construction of prospective photocatalytic materials at the atomic level on a single nanoparticle.

CRedit authorship contribution statement

W. J. Wang and X. Y. Guo proposed and conceptualized this project. S. Liu and W. J. Wang designed the experiments. S. Liu carried out the experiments and characterizations. C. T. Zhu, C. Y. Li, and W. H. Lin participated in the experiments or characterizations. S. Liu and W. J. Wang analyzed the results and drew the figures. S. Liu wrote the original draft. W. J. Wang reviewed and edited the manuscript. X. Y. Guo and Y. Yang funded this research. X. Y. Guo, Q. H. Tian, Y. Liu, and Y. Yang provided the necessary conditions for this research and participated in discussions during data analysis.

Declaration of Competing Interest

The authors declare that they have no known financial and personal relationship with other people or organizations that could inappropriately influence (bias) their work.

Acknowledgments

This work was supported by the National Natural Science Foundation of China [Grant Numbers: 51874371, 61774169] and the Qingyuan Innovation and Entrepreneurship Research Team Project [Grant Number: 2018001]. The authors would like to thank Prof. Si Xiao from the school of physics and electronics of Central South University for his kind help on carrier dynamics analysis. Besides, S. Liu and W. J. Wang would like to thank Prof. Chunhui Liu from the college of mechanical and electrical engineering of Central South University for his help on TEM characterizations.

Appendix A. Supporting information

Supplementary data associated with this article can be found in the online version at doi:10.1016/j.apcatb.2021.120909.

References

- [1] J. Gao, F. Sahli, C. Liu, D. Ren, X. Guo, J. Werner, Q. Jeangros, S.M. Zakeeruddin, C. Ballif, M. Grätzel, J. Luo, Solar water splitting with perovskite/silicon tandem cell and TiC-supported Pt nanocluster electrocatalyst, *Joule* 3 (2019) 2930–2941, <https://doi.org/10.1016/j.joule.2019.10.002>.
- [2] J. Bian, Z. Zhang, J. Feng, M. Thangamuthu, F. Yang, L. Sun, Z. Li, Y. Qu, D. Tang, Z. Lin, F. Bai, J. Tang, L. Jing, Novel energy platform for the directed charge transfer in the cascade Z-scheme heterojunction for CO₂ photoreduction without the need for a cocatalyst, *anie.202106929*, *Angew. Chem. Int. Ed.* 57 (2021) 2891–2894, <https://doi.org/10.1002/anie.202106929>.
- [3] L. Cheng, Q. Xiang, Y. Liao, H. Zhang, CdS-Based photocatalysts, *Energy Environ. Sci.* 11 (2018) 1362–1391, <https://doi.org/10.1039/C7EE03640J>.
- [4] M.G. Walter, E.L. Warren, J.R. McKone, S.W. Boettcher, Q. Mi, E.A. Santori, N. S. Lewis, Solar water splitting cells, *Chem. Rev.* 110 (2010) 6446–6473, <https://doi.org/10.1021/cr1002326>.
- [5] S. Li, P. Miao, Y. Zhang, J. Wu, B. Zhang, Y. Du, X. Han, J. Sun, P. Xu, Recent advances in plasmonic nanostructures for enhanced photocatalysis and electrocatalysis, *Adv. Mater.* 33 (2021), 2000086, <https://doi.org/10.1002/adma.202000086>.
- [6] T. Wang, Y. Chai, D. Ma, W. Chen, W. Zheng, S. Huang, Multidimensional CdS nanowire/CdIn₂S₄ nanosheet heterostructure for photocatalytic and photoelectrochemical applications, *Nano Res.* 10 (2017) 2699–2711, <https://doi.org/10.1007/s12274-017-1473-y>.
- [7] Q. Wang, T. Hisatomi, Q. Jia, H. Tokudome, M. Zhong, C. Wang, Z. Pan, T. Takata, M. Nakabayashi, N. Shibata, Y. Li, I.D. Sharp, A. Kudo, T. Yamada, K. Domen, Scalable water splitting on particulate photocatalyst sheets with a solar-to-hydrogen energy conversion efficiency exceeding 1%, *Nat. Mater.* 15 (2016) 611–615, <https://doi.org/10.1038/nmat4589>.
- [8] J. Tang, M. sheng Chu, F. Li, C. Feng, Z. gen Liu, Y. sheng Zhou, Development and progress on hydrogen metallurgy, *Int. J. Miner. Metall. Mater.* 27 (2020) 713–723, <https://doi.org/10.1007/s12613-020-2021-4>.
- [9] Y. Liao, Z. Hu, Q. Gu, C. Xue, Amine-functionalized ZnO nanosheets for efficient CO₂ capture and photoreduction, *Molecules* 20 (2015) 18847–18855, <https://doi.org/10.3390/molecules201018847>.
- [10] Y. Hu, X. Hao, Z. Cui, J. Zhou, S. Chu, Y. Wang, Z. Zou, Enhanced photocarrier separation in conjugated polymer engineered CdS for direct Z-scheme photocatalytic hydrogen evolution, *Appl. Catal. B Environ.* 260 (2020), 118131, <https://doi.org/10.1016/j.apcatb.2019.118131>.
- [11] J. Xu, W.-M. Yang, S.-J. Huang, H. Yin, H. Zhang, P. Radjenovic, Z.-L. Yang, Z.-Q. Tian, J.-F. Li, CdS core-Au plasmonic satellites nanostructure enhanced photocatalytic hydrogen evolution reaction, *Nano Energy* 49 (2018) 363–371, <https://doi.org/10.1016/j.nanoen.2018.04.048>.
- [12] S. Li, Y.H. Ng, R. Zhu, S. Lv, C. Wu, Y. Liu, L. Jing, J. Deng, H. Dai, In situ construction of elemental phosphorus nanorod-modified TiO₂ photocatalysts for efficient visible-light-driven H₂ generation, *Appl. Catal. B Environ.* 297 (2021), 120412, <https://doi.org/10.1016/j.apcatb.2021.120412>.
- [13] R.-B. Wei, Z.-L. Huang, G.-H. Gu, Z. Wang, L. Zeng, Y. Chen, Z.-Q. Liu, Dual-cocatalysts decorated rimous CdS spheres advancing highly-efficient visible-light photocatalytic hydrogen production, *Appl. Catal. B Environ.* 231 (2018) 101–107, <https://doi.org/10.1016/j.apcatb.2018.03.014>.
- [14] S. Wojtyla, T. Baran, Photocatalytic H₂ production over RuO₂@ZnS and RuO₂@CuS nanostructures, *Int. J. Hydrog. Energy* 44 (2019) 14624–14634, <https://doi.org/10.1016/j.ijhydene.2019.04.132>.
- [15] J. Pan, S. Shen, W. Zhou, J. Tang, H. Ding, J. Wang, L. Chen, C.T. Au, S.F. Yin, Recent progress in photocatalytic hydrogen evolution, *Wuli Huaxue Xuebao/Acta Phys. - Chim. Sin.* 36 (2020) 1–17, <https://doi.org/10.3866/PKU.WHXB201905068>.
- [16] Z. Wang, C. Li, K. Domen, Recent developments in heterogeneous photocatalysts for solar-driven overall water splitting, *Chem. Soc. Rev.* 48 (2019) 2109–2125, <https://doi.org/10.1039/C8CS00542g>.
- [17] X. Guo, S. Liu, W. Wang, C. Zhu, C. Li, Y. Yang, Q. Tian, Y. Liu, Enhanced photocatalytic hydrogen production activity of Janus Cu_{1.94}S-ZnS spherical nanoheterostructures, *J. Colloid Interface Sci.* 600 (2021) 838–846, <https://doi.org/10.1016/j.jcis.2021.05.073>.
- [18] K. Li, B. Peng, T. Peng, Recent advances in heterogeneous photocatalytic CO₂ conversion to solar fuels, *ACS Catal.* 6 (2016) 7485–7527, <https://doi.org/10.1021/acscatal.6b02089>.
- [19] X. He, C. Zhang, Recent advances in structure design for enhancing photocatalysis, *J. Mater. Sci.* 54 (2019) 8831–8851, <https://doi.org/10.1007/s10853-019-03417-8>.
- [20] X. Guo, S. Liu, W. Wang, C. Li, Y. Yang, Q. Tian, Y. Liu, Plasmon-induced ultrafast charge transfer in single-particulate Cu_{1.94}S-ZnS nanoheterostructures, *Nanoscale Adv.* 3 (2021) 3481–3490, <https://doi.org/10.1039/D1NA00037C>.
- [21] L. Wang, W. Wang, Y. Chen, L. Yao, X. Zhao, H. Shi, M. Cao, Y. Liang, Heterogeneous p-n Junction Cds/Cu₂O nanorod arrays: synthesis and superior visible-light-driven photoelectrochemical performance for hydrogen evolution, *ACS Appl. Mater. Interfaces* 10 (2018) 11652–11662, <https://doi.org/10.1021/acsami.7b19530>.
- [22] P. Bhavani, D.P. Kumar, H.S. Shim, P. Rangappa, M. Gopannagari, D.A. Reddy, J. K. Song, T.K. Kim, In situ addition of Ni salt onto a skeletal Cu₇S₄ integrated CdS nanorod photocatalyst for efficient production of H₂ under solar light irradiation, *Catal. Sci. Technol.* 10 (2020) 3542–3551, <https://doi.org/10.1039/c9cy02612f>.
- [23] J. Zhang, J. Yu, Y. Zhang, Q. Li, J.R. Gong, Visible light photocatalytic H₂-production activity of CuS/ZnS porous nanosheets based on photoinduced interfacial charge transfer, *Nano Lett.* 11 (2011) 4774–4779, <https://doi.org/10.1021/nl202587b>.
- [24] J. Mao, C.-T. He, J. Pei, Y. Liu, J. Li, W. Chen, D. He, D. Wang, Y. Li, Isolated Ni atoms dispersed on Ru nanosheets: high-performance electrocatalysts toward hydrogen oxidation reaction, *Nano Lett.* 20 (2020) 3442–3448, <https://doi.org/10.1021/acs.nanolett.0c00364>.
- [25] B. Qiu, Q. Zhu, M. Du, L. Fan, M. Xing, J. Zhang, Efficient solar light harvesting CdS/Cu₂S hollow cubes for Z-scheme photocatalytic water splitting, *Angew. Chem. Int. Ed.* 56 (2017) 2684–2688, <https://doi.org/10.1002/anie.201612551>.
- [26] Q. Li, X. Wang, K. Tang, M. Wang, C. Wang, C. Yan, Electronic modulation of electrocatalytically active center of Cu₂S₄ nanodisks by cobalt-doping for highly efficient oxygen evolution reaction, *ACS Nano* 11 (2017) 12230–12239, <https://doi.org/10.1021/acsnano.7b05606>.
- [27] D. Zhu, H. Ye, Z. Liu, J. Liu, H. Fu, Y. Huang, F. Teng, Z. Wang, A. Tang, Seed-mediated growth of heterostructured Cu_{1.94}S-MS (M = Zn, Cd, Mn) and alloyed CuNS₂ (N = In, Ga) nanocrystals for use in structure- and composition-dependent photocatalytic hydrogen evolution, *Nanoscale* 12 (2020) 6111–6120, <https://doi.org/10.1039/c9nr10004k>.
- [28] Y. Chen, S. Zhao, X. Wang, Q. Peng, R. Lin, Y. Wang, R. Shen, X. Cao, L. Zhang, G. Zhou, J. Li, A. Xia, Y. Li, Synergetic integration of Cu_{1.94}S-Zn₉Cd_{1-x}S heteronanorods for enhanced visible-light-driven photocatalytic hydrogen production, *J. Am. Chem. Soc.* 138 (2016) 4286–4289, <https://doi.org/10.1021/jacs.5b12666>.
- [29] W. Zhang, A.R. Mohamed, W. Ong, Z-Scheme photocatalytic systems for carbon dioxide reduction: where are we now, *Angew. Chem. Int. Ed.* 59 (2020) 22894–22915, <https://doi.org/10.1002/anie.201914925>.
- [30] S. Kai, B. Xi, X. Liu, L. Ju, P. Wang, Z. Feng, X. Ma, S. Xiong, An innovative Au-CdS/ZnS-RGO architecture for efficient photocatalytic hydrogen evolution, *J. Mater. Chem. A* 6 (2018) 2895–2899, <https://doi.org/10.1039/c7ta10958j>.
- [31] H. Feng, L. Liang, W. Wu, Z. Huang, Y. Liu, Architecting epitaxial-lattice-mismatch-free (LMF) zinc oxide/bismuth oxyiodide nano-heterostructures for efficient photocatalysis, *J. Mater. Chem. C* 8 (2020) 11263–11273, <https://doi.org/10.1039/D0TC02607G>.
- [32] Q. Yuan, D. Liu, N. Zhang, W. Ye, H. Ju, L. Shi, R. Long, J. Zhu, Y. Xiong, Noble-metal-free janus-like structures by cation exchange for Z-scheme photocatalytic water splitting under broadband light irradiation, *Angew. Chem. Int. Ed. Engl.* 56 (2017) 4206–4210, <https://doi.org/10.1002/anie.201700150>.
- [33] Y.-H. Li, M.-Y. Qi, J.-Y. Li, Z.-R. Tang, Y.-J. Xu, Noble metal free CdS@CuS-Ni₃P hybrid with modulated charge transfer for enhanced photocatalytic performance, *Appl. Catal. B Environ.* 257 (2019), 117934, <https://doi.org/10.1016/j.apcatb.2019.117934>.
- [34] Y. Dong, Y. Su, Y. Hu, H. Li, W. Xie, Ag₂S-CdS p-n nanojunction-enhanced photocatalytic oxidation of alcohols to aldehydes, *Small* 16 (2020) 1–7, <https://doi.org/10.1002/smll.202001529>.
- [35] Z. Liu, A. Tang, J. Liu, D. Zhu, X. Shi, Q. Kong, Z. Wang, S. Qu, F. Teng, Z. Wang, Non-injection synthesis of L-shaped wurtzite Cu-Ga-Zn-S alloyed nanorods and their advantageous application in photocatalytic hydrogen evolution, *J. Mater. Chem. A* 6 (2018) 18649–18659, <https://doi.org/10.1039/C8TA05395B>.
- [36] X. Zhang, Y. Guo, J. Tian, B. Sun, Z. Liang, X. Xu, H. Cui, Controllable growth of MoS₂ nanosheets on novel Cu₂S snowflakes with high photocatalytic activity, *Appl. Catal. B Environ.* 232 (2018) 355–364, <https://doi.org/10.1016/j.apcatb.2018.03.074>.
- [37] L. De Trizio, L. Manna, Forging colloidal nanostructures via cation exchange reactions, *Chem. Rev.* 116 (2016) 10852–10887, <https://doi.org/10.1021/acs.chemrev.5b00739>.
- [38] A.G. Butterfield, L.T. Alameda, R.E. Schaak, Emergence and control of stacking fault formation during nanoparticle cation exchange reactions, *J. Am. Chem. Soc.* 143 (2021) 1779–1783, <https://doi.org/10.1021/jacs.0c13072>.
- [39] J.B. Rivest, P.K. Jain, Cation exchange on the nanoscale: an emerging technique for new material synthesis, device fabrication, and chemical sensing, *Chem. Soc. Rev.* 42 (2013) 89–96, <https://doi.org/10.1039/C2CS35241A>.
- [40] B.C. Steimle, J.L. Fenton, R.E. Schaak, Rational construction of a scalable heterostructured nanorod megalibrary, *Science* 367 (2020) 418–424, <https://doi.org/10.1126/science.aaz1172>.
- [41] D. Zhu, H. Ye, Z. Liu, J. Liu, H. Fu, Y. Huang, F. Teng, Z. Wang, A. Tang, Seed-mediated growth of heterostructured Cu_{1.94}S-MS (M = Zn, Cd, Mn) and alloyed CuNS₂ (N = In, Ga) nanocrystals for use in structure- and composition-dependent photocatalytic hydrogen evolution, *Nanoscale* 12 (2020) 6111–6120, <https://doi.org/10.1039/C9NR10004K>.
- [42] G. Mumme, W. Gable, The crystal structure of roxbyte Cu₅₈S₃₂, *Can. Mineral.* 50 (2012) 423–430.
- [43] Y.-N. Xu, W.Y. Ching, Electronic, optical, and structural properties of some wurtzite crystals, *Phys. Rev. B* 48 (1993) 4335–4351, <https://doi.org/10.1103/PhysRevB.48.4335>.
- [44] H. Park, J. Kwon, J. Kim, K. Park, T. Song, U. Paik, Facile growth of metal-rich Cu_{1.75}S and Cu_{1.8}S microspheres assembled with mesoporous nanosheets and their application in Na-ion batteries, *Cryst. Growth Des.* 20 (2020) 3325–3333, <https://doi.org/10.1021/acs.cgd.0c00127>.
- [45] M.D. Regulacio, C. Ye, S.H. Lim, M. Bosman, L. Polavarapu, W.L. Koh, J. Zhang, Q. Xu, M. Han, One-pot synthesis of Cu_{1.94}S-CdS and Cu_{1.94}S-Zn₉Cd_{1-x}S nanodisk heterostructures, *J. Am. Chem. Soc.* 133 (2011) 2052–2055, <https://doi.org/10.1021/ja1090589>.
- [46] D. Ha, A.H. Caldwell, M.J. Ward, S. Honrao, K. Mathew, R. Hovden, M.K.A. Koker, D.A. Muller, R.G. Hennig, R.D. Robinson, Solid-solid phase transformations induced through cation exchange and strain in 2D heterostructured copper sulfide

- nanocrystals, *Nano Lett.* 14 (2014) 7090–7099, <https://doi.org/10.1021/nl5035607>.
- [47] M. Ye, C. Chen, N. Zhang, X. Wen, W. Guo, C. Lin, Quantum-dot sensitized solar cells employing hierarchical Cu_2S microspheres wrapped by reduced graphene oxide nanosheets as effective counter electrodes, *Adv. Energy Mater.* 4 (2014) 1–8, <https://doi.org/10.1002/aenm.201301564>.
- [48] J. Chu, X. Han, Z. Yu, Y. Du, B. Song, P. Xu, Highly efficient visible-light-driven photocatalytic hydrogen production on $\text{CdS}/\text{Cu}_2\text{S}_4/\text{g-C}_3\text{N}_4$ ternary heterostructures, *ACS Appl. Mater. Interfaces* 10 (2018) 20404–20411, <https://doi.org/10.1021/acsami.8b02984>.
- [49] B. Chong, L. Chen, D. Han, L. Wang, L. Feng, Q. Li, C. Li, W. Wang, CdS-modified one-dimensional $\text{g-C}_3\text{N}_4$ porous nanotubes for efficient visible-light photocatalytic conversion, *Chin. J. Catal.* 40 (2019) 959–968, [https://doi.org/10.1016/S1872-2067\(19\)63355-3](https://doi.org/10.1016/S1872-2067(19)63355-3).
- [50] X. Li, K. Dai, C. Pan, J. Zhang, Diethylenetriamine-functionalized CdS nanoparticles decorated on Cu_2S snowflake microparticles for photocatalytic hydrogen production, *ACS Appl. Nano Mater.* 3 (2020) 11517–11526, <https://doi.org/10.1021/acsanm.0c02616>.
- [51] M. Gopannagari, D.P. Kumar, D.A. Reddy, S. Hong, M.I. Song, T.K. Kim, In situ preparation of few-layered WS_2 nanosheets and exfoliation into bilayers on CdS nanorods for ultrafast charge carrier migrations toward enhanced photocatalytic hydrogen production, *J. Catal.* 351 (2017) 153–160, <https://doi.org/10.1016/j.jcat.2017.04.016>.
- [52] I. Vamvasakis, A. Trapali, J. Miao, B. Liu, G.S. Armatas, Enhanced visible-light photocatalytic hydrogen production activity of three-dimensional mesoporous p-CuS/n-CdS nanocrystal assemblies, *Inorg. Chem. Front.* 4 (2017) 433–441, <https://doi.org/10.1039/c6qi00515b>.
- [53] C. Li, W. Wang, Y. Yang, S. Liu, C. Zhu, Q. Tian, Core-shell $\text{Cu}_{1.94}\text{S-MnS}$ nanoheterostructures synthesized by cation exchange for enhanced photocatalytic hydrogen evolution, *CrystEngComm* 23 (2021) 6291–6299, <https://doi.org/10.1039/D1CE00717C>.
- [54] Z. Lian, M. Sakamoto, J.J.M. Vequizo, C.S.K. Ranasinghe, A. Yamakata, T. Nagai, K. Kimoto, Y. Kobayashi, N. Tamai, T. Teranishi, Plasmonic p-n junction for infrared light to chemical energy conversion, *J. Am. Chem. Soc.* 141 (2019) 2446–2450, <https://doi.org/10.1021/jacs.8b11544>.
- [55] Y. Wang, H. Mu, X. Li, J. Yuan, J. Chen, S. Xiao, Q. Bao, Y. Gao, J. He, Observation of large nonlinear responses in a graphene- Bi_2Te_3 heterostructure at a telecommunication wavelength, *Appl. Phys. Lett.* 108 (2016), 221901, <https://doi.org/10.1063/1.4953072>.
- [56] Q. Ding, Y. Shi, M. Chen, H. Li, X. Yang, Y. Qu, W. Liang, M. Sun, Ultrafast dynamics of plasmon-exciton interaction of ag nanowire- graphene hybrids for surface catalytic reactions, *Sci. Rep.* 6 (2016) 1–10, <https://doi.org/10.1038/srep32724>.
- [57] Y. Lou, X. Chen, A.C. Samia, C. Burda, Femtosecond spectroscopic investigation of the carrier lifetimes in digenite quantum dots and discrimination of the electron and hole dynamics via ultrafast interfacial electron transfer, *J. Phys. Chem. B* 107 (2003) 12431–12437, <https://doi.org/10.1021/jp035618k>.
- [58] D. Ruan, M. Fujitsuka, T. Majima, Exfoliated Mo_2C nanosheets hybridized on CdS with fast electron transfer for efficient photocatalytic H_2 production under visible light irradiation, *Appl. Catal. B Environ.* 264 (2020), 118541, <https://doi.org/10.1016/j.apcatb.2019.118541>.
- [59] L. Huang, J. Yang, X. Wang, J. Han, H. Han, C. Li, Effects of surface modification on photocatalytic activity of CdS nanocrystals studied by photoluminescence spectroscopy, *Phys. Chem. Chem. Phys.* 15 (2013) 553–560, <https://doi.org/10.1039/c2cp41153a>.
- [60] M. Liu, Y. Liu, B. Gu, X. Wei, G. Xu, X. Wang, M.T. Swihart, K.T. Yong, Recent advances in copper sulphide-based nanoheterostructures, *Chem. Soc. Rev.* 48 (2019) 4950–4965, <https://doi.org/10.1039/c8cs00832a>.
- [61] J.A. Nasir, Z.U. Rehman, S.N.A. Shah, A. Khan, I.S. Butler, C.R.A. Catlow, Recent developments and perspectives in CdS-based photocatalysts for water splitting, *J. Mater. Chem. A* 8 (2020) 20752–20780, <https://doi.org/10.1039/d0ta05834c>.
- [62] Y. Li, Y. Hu, S. Peng, G. Lu, S. Li, Synthesis of CdS nanorods by an ethylenediamine assisted hydrothermal method for photocatalytic hydrogen evolution, *J. Phys. Chem. C* 113 (2009) 9352–9358, <https://doi.org/10.1021/jp901505j>.